



Microscopy of an ultranarrow Feshbach resonance using a laser-based atom collider: A quantum defect theory analysis

Matthew Chilcott ¹, James F. E. Croft ¹, Ryan Thomas ^{1,2} and Niels Kjaergaard ^{1,*}

¹*Department of Physics, Quantum Science Otago, and Dodd-Walls Centre for Photonic and Quantum Technologies, University of Otago, Dunedin 9016, New Zealand*

²*Department of Quantum Science and Technology, Research School of Physics, The Australian National University, Canberra 2601, Australia*



(Received 7 February 2022; accepted 9 June 2022; published 4 August 2022)

We employ a quantum defect theory framework to provide a detailed analysis of the interplay between a magnetic Feshbach resonance and a shape resonance in cold collisions of ultracold ^{87}Rb atoms as captured in recent experiments using a laser-based collider [M. Chilcott *et al.*, *Phys. Rev. Research* **3**, 033209 (2021)]. By exerting control over a parameter space spanned by both collision energy and magnetic field, the width of a Feshbach resonance can be tuned over several orders of magnitude. We apply a quantum defect theory specialized for ultracold atomic collisions to fully describe of the experimental observations. While the width of a Feshbach resonance generally increases with collision energy, its coincidence with a shape resonance leads to a significant additional boost. By conducting experiments at a collision energy matching the shape resonance and using the shape resonance as a magnifying lens, we demonstrate a feature broadening to a magnetic width of 8 G compared to a predicted Feshbach resonance width much less than 0.1 mG.

DOI: [10.1103/PhysRevA.106.023303](https://doi.org/10.1103/PhysRevA.106.023303)

I. INTRODUCTION

Collisional resonances are ubiquitous in atomic and particle physics, where they arise due to coupling between the scattering continuum and a quasibound state. Their telltale signature is an abrupt suppression or enhancement in scattering as the collision energy is scanned, but they may also emerge when scanning an external field which tunes the energy levels of the system. In ultracold atomic physics, such field-tunable resonances provide an indispensable tool for manipulating the interactions between atoms, which has been exploited in a number of hallmark quantum experiments in atomic systems, including solitons [1], the BEC-BCS crossover [2,3], and quantum droplets [4].

With the recent push towards experiments with ultracold molecules [5,6], the interaction between collisional resonances has become a subject of increased interest, due to the high density of states in molecules compared to atoms. Extraordinarily long lifetimes, approaching milliseconds [7–9], have been observed in collisions between nonreactive ultracold molecules in their absolute ground state. These long lifetime have been attributed to the high density of states of molecules [10–12] and suggest the presence of overlapping resonances [13]. Interacting Feshbach resonances are also of importance in collisions of ultracold magnetic lanthanides, such as erbium and dysprosium, and have been used to reveal the chaotic nature of the collision process [14,15].

Multichannel quantum defect theory (MQDT) was originally developed to describe an electron moving in a long-range Coulomb potential (see [16] and references therein).

This was later generalized to treat scattering problems involving broader classes of potentials including the long-range van der Waals interaction for atomic collisions [17–22]. For the low energies characteristic of scattering in the cold and ultracold domain, MQDT has proven particularly fruitful, capturing the physics at threshold [23–32]. By separating the scattering problem into energy sensitive and insensitive components, quantum defect theory (QDT) allows for an elegant description of resonance interactions, with the energy dependence encapsulated in a few analytic parameters. Recent demonstrations of the power of QDT include the prediction and interpretation of triplet structures for d -wave Feshbach resonances [33] and shape resonances [34].

In this paper we study the interaction between a shape resonance and a Feshbach resonance in collisions of ^{87}Rb atoms, with both resonances arising from quasibound d -wave states of the system. Figure 1 shows an example potential well for the collisional entrance channel (blue line) which describes the interaction as a function of radial separation. When including angular momentum, the effective potential contains a barrier in front of the potential well (orange line), behind which a quasibound state can be formed (orange dashed line). For atoms tunneling through the barrier, such a quasibound state gives rise to a scattering resonance. Similarly, Feshbach resonances arise from the coupling to a bound state, but in this case the bound state belongs to a closed channel. A closed-channel potential, which is energetically inaccessible for separated particles, is presented in red in Fig. 1. Due to the deep potential well, the closed channel shown becomes accessible at short range during a collision. If a bound state (red dashed line) is present at the collision energy, incoming atoms can temporarily bind in this state, enhancing their interaction. In the case of a magnetic Feshbach resonance, the different

*niels.kjaergaard@otago.ac.nz

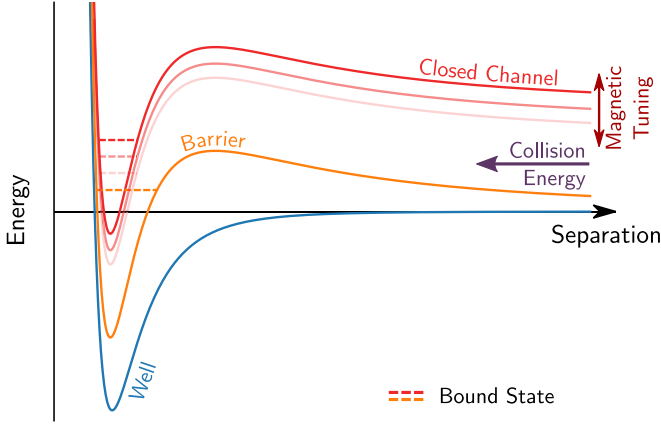


FIG. 1. Representative interaction potentials. The s -wave channel is shown by the blue solid curve. The addition of d -wave angular momentum gives rise to a potential (orange solid curve), with a barrier hosting a quasibound state (dashed orange line). The centrifugal barrier is highly exaggerated to be visible; in reality its height is orders of magnitude smaller than the depth of the well. We also show the potential of a closed-channel potential in red, also with d -wave character and hosting a bound state (dashed red line). The relative position of the closed channel can be tuned with a magnetic field, and the bound state associated with the Feshbach resonance can be pulled through the shape resonance.

magnetic moments of the closed and entrance channels allow us to manipulate the position of the Feshbach resonance in energy.

While shape resonances and Feshbach resonances are typically treated in isolation, the tunability of the latter opens up the possibility of moving a Feshbach resonance through a shape resonance using an external field. We recently studied the interaction of a pair of such resonances and observed the avoided crossing in the associated S matrix poles [35]. In the present work we revisit the data acquired in these experiments and extend our analysis of this resonance pair to give an interpretation in terms of multichannel quantum defect theory. We show that a simple two-channel QDT model captures all the essential physics of the interacting collisional resonances.

II. EXPERIMENTAL METHODS

A. System

We collide pairs of ^{87}Rb atoms, both of which are in the absolute ground hyperfine state $|F, m_F\rangle = |1, 1\rangle$. This $|1, 1\rangle|1, 1\rangle$ entrance channel has a plethora of Feshbach resonances, previously mapped out by loss spectroscopy [36]. In the present study, we utilize a d -wave Feshbach resonance corresponding to the closed-channel molecular state with the quantum numbers $F_1 = 2, F_2 = 2, v' = -5$, and $M = 2$, where $M = m_{F_1} + m_{F_2}$ and v' is the vibrational quantum number counting from the $F_1 = 2, F_2 = 2$ threshold. For a magnetic field of 930 G, this state is located at the $|1, 1\rangle|1, 1\rangle$ -channel threshold where it is predominantly comprised of components from the $|2, 0\rangle|2, 2\rangle$ and $|2, 1\rangle|2, 1\rangle$ channels. The $|1, 1\rangle|1, 1\rangle$ channel also hosts a d -wave shape resonance at a collision energy near $300 \mu\text{K}$ [37,38], as measured in units of the Boltzmann constant k_B .

The Feshbach resonance we employ was predicted by Marte *et al.* [36] to be located at 930.9 G with a theoretical width much less than 0.1 mG; their experiments observed it at $B_0 = 930.02$ G using loss spectroscopy. A subsequent observation has placed this resonance at 930.89 G in photoassociation experiments [39]. Our own loss spectroscopy measurements (described in Appendix A) observe the zero-energy resonance at 929.921(3) G.

B. Optical collider

Our collider is composed of a system of steerable optical dipole traps, formed by pairs of crossed red-detuned laser beams [40]. The procedure to prepare two ultracold (~ 800 nK) $|1, 1\rangle$ -state ^{87}Rb clouds in separate crossed dipole traps is detailed in [35]. We tune the position of the Feshbach resonance by applying a magnetic field with a pair of Helmholtz coils carrying a current controlled at the ppm level [41], before accelerating the two clouds, each containing $\sim 3 \times 10^5$ atoms, to collide at a specific energy in the range $156\text{--}850 \mu\text{K}$. The acceleration is achieved by steering the laser trapping beams and as the clouds reach the collision energy, all laser beams are turned off so that the atoms collide in the absence of trapping.

C. Detection

After the clouds separate postcollision, we acquire an absorption image of the clouds and the halo of scattered atoms. Figure 2(a) shows examples of such images with the atom distribution projected onto a plane and exhibiting clear d -wave character [37,42]. We integrate the image [Fig. 2(b)] in the direction orthogonal to the collision (vertically) and the resulting integral [Fig. 2(c)] carries a spatial imprint of shapes associated with the interfering s and d partial waves, and the unscattered thermal clouds. By fitting these shapes to the integrated image, we extract the scattered fraction \mathcal{S} .

The cross section is related to the scattered fraction by [43]

$$\mathcal{S} = \frac{\alpha\sigma}{1 + \alpha\sigma}, \quad (1)$$

where $\sigma = \sigma_s + \sigma_d$ is the sum of the s and d partial-wave cross sections and the parameter α is geometry dependent and left as a free parameter when fitting the cross section. For a particular partial wave ℓ , the cross section is

$$\sigma_\ell = \frac{4\pi\hbar^2(2\ell + 1)}{\mu E} \sin^2(\delta_\ell), \quad (2)$$

where δ_ℓ is the corresponding partial wave scattering phase shift, E is the collision energy, and μ is the reduced mass. As we are colliding indistinguishable bosons, only even- ℓ partial waves are allowed and Eq. (2) includes an additional factor of 2 compared to the distinguishable particle case. Because the magnetic Feshbach resonance has a d -wave character, we take the s -wave phase shift δ_s and consequently σ_s to be constant in magnetic field and only a function of energy. Close to the magnetic resonance, the d -wave phase shift δ_d can be described by the Beutler-Fano model

$$\delta_d(E, B) = \delta_{\text{bg}}(E) + \arctan\left(\frac{\Gamma_B(E)/2}{B - B_{\text{res}}(E)}\right), \quad (3)$$

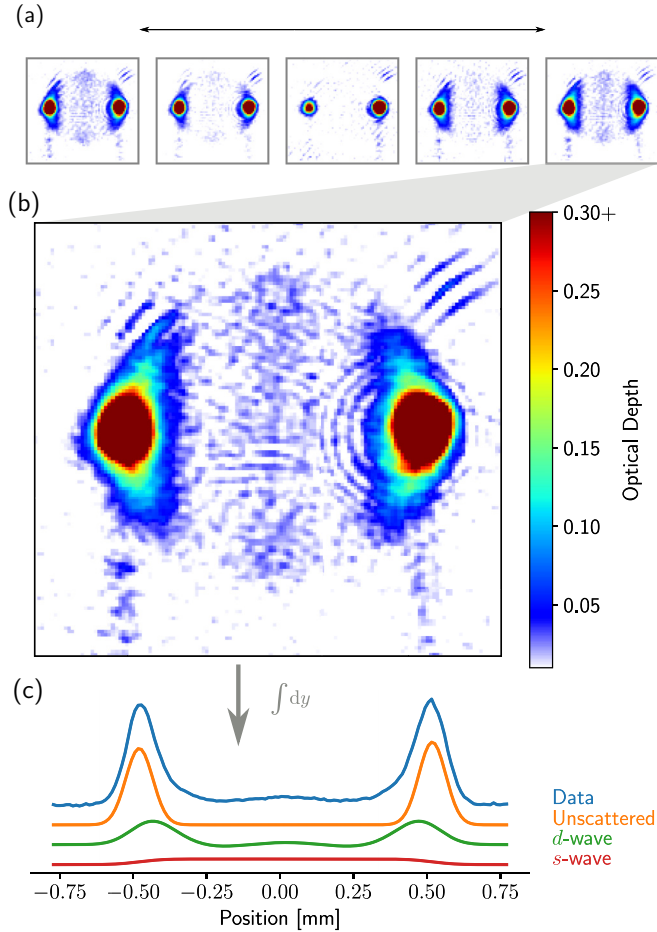


FIG. 2. Fractions of scattered atoms from postcollision absorption images. (a) Absorption images at a range of magnetic fields over the resonance for a collision energy of $E/k_B = 270 \mu\text{K}$. The collision axis is horizontal. (b) Close-up of a collision near 940 G. The scattering here is strongly anisotropic and has the signature of d -wave scattering [42]. (c) Integrated column density [blue (top) curve], to which our model is fitted in order to extract the parameters of the collision. From the fit the components of unscattered (orange curve) and the s -wave (red curve) and d -wave (green curve) scattered atoms are extracted.

for a magnetic field B and a collision energy E . With this resonance model, we extract the d -wave background phase shift $\delta_{\text{bg}}(E)$ along with the width $\Gamma_B(E)$ and position $B_{\text{res}}(E)$ of the Fano line shape by sweeping the magnetic field at constant energy.

The Beutler-Fano model above is equivalent to the common form of the Fano profile [44]

$$\sigma \propto \frac{(q + \epsilon)^2}{1 + \epsilon^2}, \quad (4)$$

where q is the so-called shape parameter and ϵ is the scaled dimensionless parameter in which the resonance occurs. In our case, the required mapping to this form is given by $q = \cot(\delta_{\text{bg}})$ and $\epsilon = 2(B - B_{\text{res}})/\Gamma_B$, the inverse of the arctan argument in Eq. (3). Representative Fano profiles measured at four different energies are shown in Fig. 3, illustrating different regimes of the q parameter.

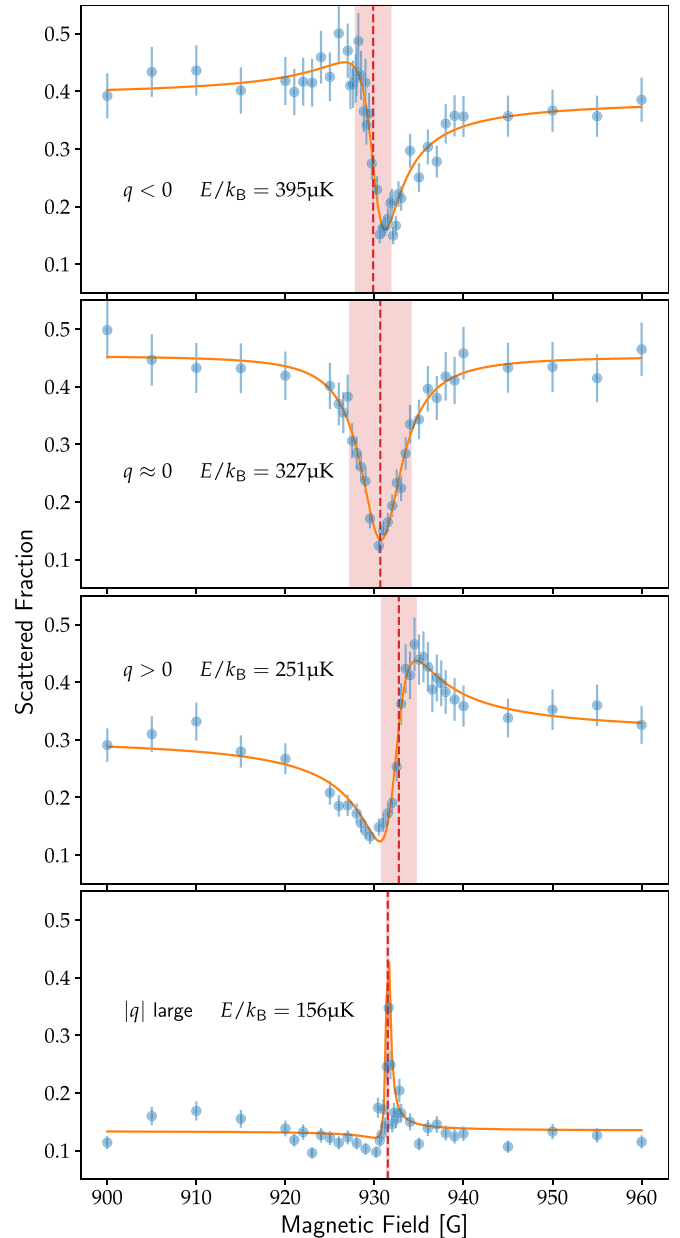


FIG. 3. Examples of Fano profiles of differing shape parameters q as encountered in our experiments. Points show the measured scattered fraction as a function of magnetic field for four different collision energies E . The solid lines are curve fits based on the Beutler-Fano model outlined in Sec. II C. The fitted parameters B_{res} and Γ_B [cf. Eq. (3)] are indicated as a dashed line and a shaded area, respectively. The experimental data illustrating the characteristic Fano profiles were previously published in [35].

The line shape parametrized by q can be thought of as due to the interference between the two pathways; the asymmetric line shape then arises due to the constructive interference on one side and destructive interference on the other [45,46].

We note that the limiting cases provide a symmetric dip at $q = 0$ and a Lorentzian profile at $|q| \rightarrow \infty$, while intermediate values of q are tied to asymmetric profiles with a “polarity” determined by the sign of q .

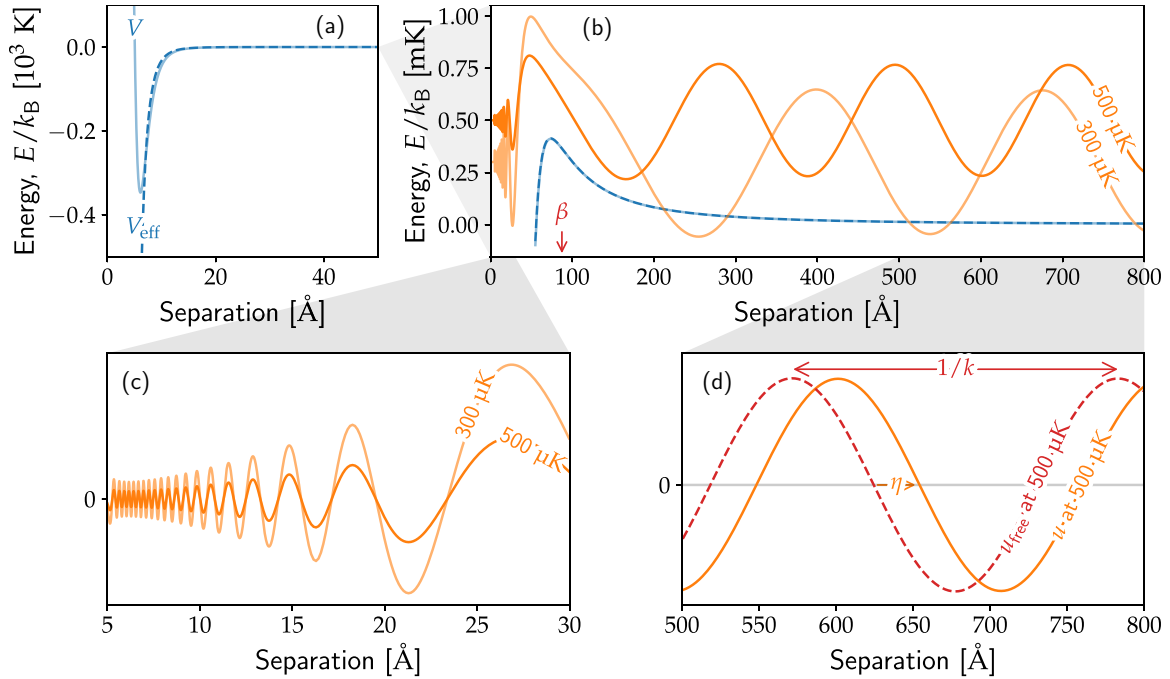


FIG. 4. Different length and energy scales of the scattering problem in the $\ell = 2$ entrance channel. (a) Triplet potential of the entrance channel V from Ref. [50]. At the long range, V is well approximated by the van der Waals potential V_{eff} . (b) At threshold and over a wider range of separation, we show two scattering wave functions derived from coupled-channel calculations, offset vertically by their collision energies. An arrow labels the length scale of the van der Waals potential β . (c) At short range, the shape of the wave function is independent of energy apart from variations of the amplitude. The increase in amplitude demonstrated at $300 \mu\text{K}$ is associated with the nearby shape resonance. (d) Scattering wave function u at long range along with the free-particle wave function u_{free} . The difference between the two is captured by a phase shift η .

III. QUANTUM DEFECT THEORY

The compelling variation in the Fano profiles observed in Fig. 3 results from the interplay between the Feshbach resonance and a shape resonance. We employ quantum defect theory to characterize and interpret the intriguing resonant scattering behavior. As mentioned in the Introduction, QDT is a well-developed theory. There are however different notations (most notably those of Greene *et al.* [19] and Mies [20]) and approximations employed by various QDT treatments. As such, here we provide a self-contained treatment which combines the numerically stable approach of Ruzic *et al.* [47] with a reference function optimization [48]. The importance of optimized reference functions in the analysis of Feshbach resonances in ultracold atomic collisions was discussed previously by Osséni *et al.* [49].

A. Overarching QDT framework

The QDT approach to cold collisions takes advantage of the separation of energy and length scales common in scattering problems [16,19,20,25,28]. The blue solid lines in Figs. 4(a) and 4(b) show the triplet interaction potential between two ^{87}Rb atoms as a function of separation. Asymptotically, this potential goes to zero. Atoms at short range [Fig. 4(a)] encounter a potential with a depth on the order of 1000 K, compared to a collision energy of the order of 1 mK. This separation of energy and length scales allows the important physics of collisions to be captured by a few

analytic parameters [29–32,51]. Importantly, computing these QDT parameters for a system only requires the long-range form of the interaction potential and the masses of the atoms.

To set the scene, we show in Fig. 4(b) the energy-normalized scattering wave functions in the $|1, 1\rangle|1, 1\rangle$ channel, generated by full coupled-channel calculations¹ at two different energies ($E/k_B = 300$ and $500 \mu\text{K}$). These wave functions highlight two salient features shared by all scattering solutions. First, inside the well solutions are oscillatory with a varying local wave number which, crucially, has virtually no dependence on the collision energy E ; the common waveforms differ only in amplitude [see Fig. 4(c)]. This difference in amplitude arises due to the asymptotic energy normalization. Second, the long-range asymptotic solutions are sinusoidal with a constant wave number. This wave number will depend strongly, but trivially, on the collision energy E as $k = \sqrt{2\mu E/\hbar^2}$ and for a given energy the sinusoid will display a phase shift $\eta(E)$ with respect to the regular free-space solution at that energy [Fig. 4(d)]. Because the specific wave functions in Fig. 4 satisfy the physical boundary conditions of the scattering problem, the partial (elastic) scattering cross section is determined by this phase shift using Eq. (2), with $\delta_\ell = \eta$. By observing that all scattering solutions share

¹The coupled-channel calculations, as used in Ref. [35], are generated by propagating the log-derivative of the wave function using the technique of Ref. [52] and extracting the wave function using the technique of Ref. [53].

some common ground via the two features highlighted above, the QDT framework will enable us to predict the energy dependence of the phase shift analytically.

1. Coupled-channel equations, \mathbf{K} matrix, and \mathbf{S} matrix

The objective of any scattering problem is to obtain the system's \mathbf{S} matrix, as it completely describes the outcome of a scattering experiment. Formally, the \mathbf{S} matrix can be constructed from computed wave functions, which are solutions to the coupled radial Schrödinger equations

$$\sum_{j=1}^N \left\{ \left[-\frac{\hbar^2}{2\mu} \frac{d^2}{dr^2} + \frac{\ell(\ell+1)\hbar^2}{2\mu r^2} \right] \delta_{ij} + V_{ij}(r) \right\} u_j(r) = E_i u_i(r), \quad (5)$$

where the energy E_i for a channel i is measured with respect to its threshold and V_{ij} are the elements of a potential matrix. In our experiments, we consider two atoms entering as $|1, 1\rangle|1, 1\rangle$. If we ignore the weak spin-spin dipole interactions, collisions between atoms 1 and 2 conserve $m_{F_1} + m_{F_2} = 2$ as well as mechanical angular momentum ℓ [54]. For the d -wave channel, their coupling is restricted to the channels $|1, 1\rangle|2, 1\rangle$, $|1, 0\rangle|2, 2\rangle$, $|2, 0\rangle|2, 2\rangle$, and $|2, 1\rangle|2, 1\rangle$ with $\ell = 2$, which results in an $N = 5$ channel set of equations [27]. Designating the entrance channel $|1, 1\rangle|1, 1\rangle$ with $i = 1$, we have $E_1 > 0$ as the asymptotically free incoming $|1, 1\rangle$ atoms have a nonzero relative kinetic energy. In our experiment the collision energy is so low that $E_i < 0$ for the remaining four channels; these are all energetically closed and atoms can only leave the collision via the $i = 1$ channel.

Generally, when solving coupled-channel problems like Eq. (5), one typically propagates out an $N \times N$ regular solution matrix² \mathbf{F} , where $N = N_o + N_c$ is the sum of the number of open and closed channels. The N columns of \mathbf{F} represent N linearly independent solution vectors to Eq. (5) with row i of a solution vector corresponding to the channel i . Asymptotically, the solution matrix can be decomposed as [55]

$$\mathbf{F}(r) \stackrel{r \rightarrow \infty}{\sim} \mathcal{J}(r) + \mathcal{N}(r)\mathbf{K}, \quad (6)$$

where \mathbf{K} is a constant real symmetric matrix and \mathcal{J} and \mathcal{N} are diagonal matrices with entries

$$\mathcal{J}_{ii}(r) = \begin{cases} r k_i^{1/2} j_\ell(k_i r) & \text{for } i \text{ open} \\ (k_i r)^{-1/2} \mathcal{I}_{\ell+1/2}(k_i r) & \text{for } i \text{ closed,} \end{cases} \quad (7a)$$

$$\mathcal{N}_{ii}(r) = \begin{cases} r k_i^{1/2} n_\ell(k_i r) & \text{for } i \text{ open} \\ (k_i r)^{-1/2} \mathcal{K}_{\ell+1/2}(k_i r) & \text{for } i \text{ closed.} \end{cases} \quad (7b)$$

Here j_ℓ and n_ℓ are spherical Bessel functions of the first and the second kind, respectively, and $\mathcal{I}_{\ell+1/2}$ and $\mathcal{K}_{\ell+1/2}$ are modified Bessel functions of the first and the third kind, respectively.

The energy-dependent \mathbf{K} matrix defined by Eq. (6) contains all the scattering behavior of the system. In particular, the $N_o \times N_o$ submatrix of \mathbf{K} that pertains to only the open channels defines the \mathbf{S} matrix [55–57]

$$\mathbf{S} = (1 + i\mathbf{K}_{oo})(1 - i\mathbf{K}_{oo})^{-1}. \quad (8)$$

²In practice, for reasons of numerical stability, it is more common to propagate the log-derivative of this matrix.

We note that \mathbf{K}_{oo} is known as the reactance matrix in the literature. In the treatment of identical particles, the wave functions must be properly symmetrized [58]. Because we only consider elastic collisions, we simply need to include a factor of 2 in the even- ℓ partial-wave cross sections [cf. Eq. (2)].

2. QDT treatment: Uncoupled channels at long range

Rather than numerically solving Eq. (5) directly to in turn obtain \mathbf{K} and \mathbf{S} , QDT proceeds by assuming that beyond a certain separation R_{int} all channels are uncoupled. Beyond this distance, the radial wave function for the entrance channel is therefore a solution to the radial Schrödinger equation

$$\left[-\frac{\hbar^2}{2\mu} \frac{d^2}{dr^2} + \frac{\ell(\ell+1)\hbar^2}{2\mu r^2} + V_1(r) \right] u_1(r) = E_1 u_1(r). \quad (9)$$

For our system, the long-range behavior of V_1 is well described by a van der Waals potential $V_1(r) = -C_6/r^6$ and Eq. (9) takes the specific form

$$\frac{d^2}{dR^2} u_1(R) = \left(\underbrace{-\frac{1}{R^6} + \frac{\ell(\ell+1)}{R^2}}_{V_{\text{eff}}(R)} - \bar{E}_1 \right) u_1(R), \quad (10)$$

where the radial distance R is measured in units of the van der Waals radius $\beta \equiv (2\mu C_6/\hbar^2)^{1/4}$ and energy on a scale $E_\beta \equiv \hbar^2/2\mu\beta^2$. We also define the local wave number

$$\bar{k}_1(R) = \sqrt{\bar{E}_1 - V_{\text{eff}}(R)}. \quad (11)$$

For reference, we note that our particular system has $C_6 = 3.253 \times 10^7 \text{ K } \text{\AA}^6$ for ^{87}Rb [59], which gives $\beta = 87.37 \text{ \AA}$ and $E_\beta = 73.11 \text{ } \mu\text{K}$.

B. QDT reference functions

Knowing that our long-range behavior is well described by the van der Waals potential, we compute the QDT reference functions in this potential.

1. Asymptotic considerations ($R \rightarrow \infty$)

As $R \rightarrow \infty$, V_{eff} vanishes and the \bar{E}_1 term on the right-hand side of Eq. (10) dominates. In this region an energy-normalized solution $u_1(R)$ is sinusoidal, oscillating with the asymptotic wave number $\bar{k}_1 \stackrel{R \rightarrow \infty}{\sim} \sqrt{\bar{E}_1}$:

$$u_1(R) \stackrel{R \rightarrow \infty}{\sim} \frac{1}{\sqrt{\bar{k}_1}} \sin(\bar{k}_1 R - \ell\pi/2 + \eta_1), \quad (12)$$

where the $\ell\pi/2$ term references the phase shift η_1 against the regular free-particle solution for the given partial wave,

$$u_{\text{free}}(R) = \bar{k}_1 R j_\ell(\bar{k}_1 R) \stackrel{R \rightarrow \infty}{\sim} \sin(\bar{k}_1 R - \ell\pi/2). \quad (13)$$

Equivalently, Eq. (12) can be written as

$$u_1(R) \stackrel{R \rightarrow \infty}{\sim} c_1 \frac{1}{\sqrt{\bar{k}_1}} \sin(\bar{k}_1 R - \ell\pi/2 + \xi_1) + c_2 \frac{1}{\sqrt{\bar{k}_1}} \cos(\bar{k}_1 R - \ell\pi/2 + \xi_1), \quad (14)$$

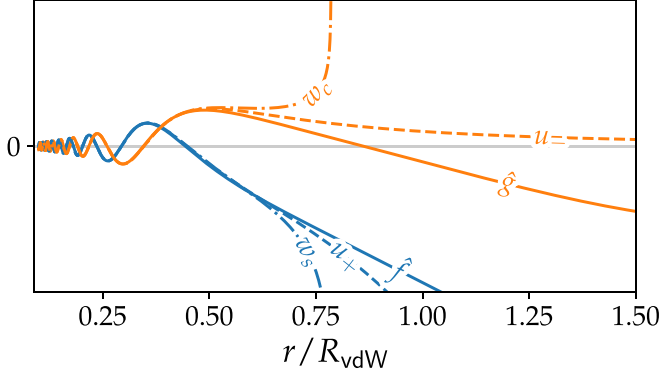


FIG. 5. Solution pairs inside the van der Waals radius: the zero-energy analytic solutions u_{\pm} , the WKB solutions w_s and w_c for $\phi_1 = 0$ (computed using $R_0 = 0.1$) at $E/k_B = 300 \mu\text{K}$, and the corresponding reference functions \hat{f}_1 and \hat{g}_1 .

where the coefficients for the two quadrature components are given by

$$\begin{bmatrix} c_1 \\ c_2 \end{bmatrix} = \begin{bmatrix} \sin \xi_1 & \cos \xi_1 \\ (-1)^\ell \cos \xi_1 & (-1)^{\ell+1} \sin \xi_1 \end{bmatrix} \begin{bmatrix} \sin \eta_1 \\ \cos \eta_1 \end{bmatrix} \quad (15)$$

for a particular choice of the arbitrary phase ξ_1 . Guided by Eq. (14), the solution of Eq. (10) can be expressed as

$$u_1(R) = c_1 f_1(R) + c_2 g_1(R), \quad (16)$$

where f_1 and g_1 are exact solutions to Eq. (10) defined by the boundary conditions

$$f_1(R) \stackrel{R \rightarrow \infty}{\sim} \frac{1}{\sqrt{\bar{k}_1}} \sin(\bar{k}_1 R - \ell\pi/2 + \xi_1) \quad (17a)$$

and

$$g_1(R) \stackrel{R \rightarrow \infty}{\sim} \frac{1}{\sqrt{\bar{k}_1}} \cos(\bar{k}_1 R - \ell\pi/2 + \xi_1). \quad (17b)$$

In Eq. (16) the coefficients c_1 and c_2 depend on the choice of the free parameter ξ_1 . In particular, for $\xi_1 = \eta_1$, $c_1 = 1$ and $c_2 = 0$.

2. Considerations inside the van der Waals radius ($R \lesssim 1$)

For $R \lesssim 1$, the \bar{E}_1 term of Eq. (10) is negligible and the solution $u_1(r)$ becomes reminiscent of the solution $u_1^{(0)}(r)$ of the Bessel equation

$$\frac{d^2}{dR^2} u_1^{(0)}(R) = - \left[\frac{1}{R^6} - \frac{\ell(\ell+1)}{R^2} \right] u_1^{(0)}(R). \quad (18)$$

Here $u_1^{(0)}(r)$ can be expressed as a linear combination of

$$u_+(R) \equiv \frac{\sqrt{\pi}}{2} \sqrt{R} Y_{(2\ell+1)/4} \left(\frac{1}{2R^2} \right) \quad (19a)$$

and

$$u_-(R) \equiv \frac{\sqrt{\pi}}{2} \sqrt{R} J_{(2\ell+1)/4} \left(\frac{1}{2R^2} \right), \quad (19b)$$

where J and Y are Bessel functions of the first and the second kind, respectively. In Fig. 5 we plot $u_{\pm}(R)$ for $\ell = 2$ and it can be seen how u_- decays as R increases, while u_+ blows

up. This functional behavior is also captured by the limiting forms [60]

$$u_+(R) \sim \begin{cases} R^{3/2} \sin\left(\frac{1}{2R^2} - \frac{2\ell+3}{8}\pi\right) & \text{for } R \rightarrow 0 \\ \frac{\sqrt{\pi}}{2} R^{\ell+1} & \text{for } R \rightarrow \infty, \end{cases} \quad (20a)$$

$$u_-(R) \sim \begin{cases} R^{3/2} \cos\left(\frac{1}{2R^2} - \frac{2\ell+3}{8}\pi\right) & \text{for } R \rightarrow 0 \\ \frac{\sqrt{\pi}}{2} R^{-\ell} & \text{for } R \rightarrow \infty. \end{cases} \quad (20b)$$

Both $u_-(R)$ and $u_+(R)$ are exact solutions to Eq. (18), i.e., Eq. (10) with $\bar{E}_1 = 0$, valid for all R . For $E > 0$, a pair of linearly independent approximate WKB solutions to Eq. (10) around some point R_0 where the potential V_{eff} is deep are given by

$$w_s(R) = \frac{1}{\sqrt{\bar{k}_1(R)}} \sin[\theta_{\text{WKB}}(R)], \quad (21a)$$

$$w_c(R) = \frac{1}{\sqrt{\bar{k}_1(R)}} \cos[\theta_{\text{WKB}}(R)], \quad (21b)$$

where

$$\theta_{\text{WKB}}(R) = - \int_{R_0}^R dR' \bar{k}_1(R') + \frac{1}{2} R_0^{-2} - \frac{2\ell+3}{8} \pi + \phi_1. \quad (22)$$

We note that in the vicinity of R_0 (i.e., for values of R where the potential well is deep), $w_s(R)$ and $w_c(R)$ are largely insensitive to the channel energy \bar{E}_1 and that for $\phi_1 = 0$ they match the analytic zero-energy solutions $u_{\pm}(R)$ in this region (Fig. 5 shows w_s and w_c for $E/k_B = 300 \mu\text{K}$). The phase ϕ_1 is the key that unlocks QDT's use of only the long-range potential because it can encapsulate the effects of the complicated multichannel short-range interaction as a scalar quantity which varies only weakly with energy and hence can be taken to be constant.

Analogous to Eq. (16), the solution $u_1(R)$ to Eq. (10) can be expressed as the linear combination

$$u_1(R) = \hat{c}_1 \hat{f}_1(R) + \hat{c}_2 \hat{g}_1(R), \quad (23)$$

where \hat{f}_1 and \hat{g}_1 are exact solutions to Eq. (10) defined by the initial values

$$\{\hat{f}_1(R_m) = w_s(R_m), \hat{f}'_1(R_m) = w'_s(R_m)\}, \quad (24a)$$

$$\{\hat{g}_1(R_m) = w_c(R_m), \hat{g}'_1(R_m) = w'_c(R_m)\}, \quad (24b)$$

where $R_m > R_{\text{int}}$ is some point within the potential well (possibly, but not necessarily R_0), and the coefficients \hat{c}_1 and \hat{c}_2 are determined by the boundary conditions of the physical problem. Individually, \hat{f}_1 and \hat{g}_1 inherit the energy insensitivity of w_s and w_c inside the potential well.

Figure 5 shows that \hat{f} and \hat{g} are perfectly tailored to represent the short-range multichannel wave function. Over the range of collision energies of interest they are essentially independent of energy, and the similarity in the wave functions at short range extends analytically to energies below threshold. The functions w_s and \hat{f}_1 , which are plotted in Fig. 5 for an energy $E/k_B = 300 \mu\text{K}$, are both completely equivalent to the zero-energy solution u_+ at short range; likewise, w_c and \hat{g}_1 are completely equivalent to the zero-energy solution u_- . We also note that, by construction, for $\phi_1 = 0$, \hat{g}_1 links up to the purely decaying zero-energy solution to Eq. (18), namely, u_- . This

choice provides numerically stable reference functions as it corresponds to propagating the maximally linearly independent pair [47].

3. Relating reference functions

The considerations of Secs. III B 1 and III B 2 provide the two pairs of reference functions $\{f_1(R), g_1(R)\}$ and $\{\hat{f}_1(R), \hat{g}_1(R)\}$, respectively. These are all defined for all $R > R_m$, but while f_1 and g_1 refer to asymptotic boundary conditions at long range, \hat{f}_1 and \hat{g}_1 refer to boundary conditions within the van der Waals radius. Connecting the pairs of reference functions defines the QDT parameters which underpin the QDT framework.

Like $f_1(R)$, the solution $\hat{f}_1(R)$ [subject to Eq. (24a) and tied to the phase ϕ_1] will be sinusoidal for $R \rightarrow \infty$. The phases of the two waveforms can be made to match through the free phase³ ξ_1 and the amplitudes can be matched by scaling $\hat{f}_1(R)$ by a factor C_1^{-1} ,

$$f_1(R) = C_1^{-1} \hat{f}_1(R). \quad (25)$$

With both ξ_1 and C_1 fixed, $g_1(R)$ can be written as a linear combination of $\hat{f}_1(R)$ and $\hat{g}_1(R)$,

$$g_1(R) = C_1 \tan \lambda_1 \hat{f}_1(R) + C_1 \hat{g}_1(R), \quad (26)$$

as \hat{f}_1 and \hat{g}_1 span the solution space. Expressions for the QDT parameters can be found by considering Wronskians of appropriate pairs of reference functions (see Appendix B 1). We note that connecting $\{f_1(R), g_1(R)\}$ and $\{\hat{f}_1(R), \hat{g}_1(R)\}$ as in the above imposes a fixed relationship between ϕ_1 and ξ_1 at a particular energy and that the QDT parameters C_1 and $\tan \lambda_1$ describing the transformation

$$\begin{bmatrix} f_1 \\ g_1 \end{bmatrix} = \begin{bmatrix} C_1^{-1} & 0 \\ C_1 \tan \lambda_1 & C_1 \end{bmatrix} \begin{bmatrix} \hat{f}_1 \\ \hat{g}_1 \end{bmatrix} \quad (27)$$

will depend on the choice of these interrelated phases.

The above procedure for connecting up reference functions introduces C_1 and $\tan \lambda_1$ as the QDT parameters for the $i = 1$ open entrance channel. To tie the QDT description to our physical system, we will (eventually) pick the pair of ϕ_1 and ξ_1 such that ξ_1 reproduces the nonresonant scattering phase shift δ_{bg} [cf. Eq. (3)]. For this choice, $c_2 = 0$ in Eq. (16), which renders f as the scattering wave function in the nonresonant scenario. As such, C_1^{-2} is the probability for the two atoms to penetrate to short range in the absence of interchannel coupling, while λ_1 is the phase lag between g_1 and \hat{g}_1 due to the difference in kinetic energy at long range compared to short range. Together, the parameters C_1 and $\tan \lambda_1$ quantify the breakdown of the WKB approximation [cf. Eq. (21)] near threshold: At energies well above threshold $C_1 \rightarrow 1$ and $\tan \lambda_1 \rightarrow 0$ as the WKB treatment becomes evermore valid at all separation ranges.

C. Multichannel QDT

In general, any open channel i of a system can be subjected to the considerations for $i = 1$ above. The rationale behind

defining \hat{f}_i and \hat{g}_i following the prescription of Sec. III B 2 with a corresponding transformation

$$\begin{bmatrix} f_i \\ g_i \end{bmatrix} = \begin{bmatrix} C_i^{-1} & 0 \\ C_i \tan \lambda_i & C_i \end{bmatrix} \begin{bmatrix} \hat{f}_i \\ \hat{g}_i \end{bmatrix} \quad (28)$$

becomes clear if we write the full complicated many-channel radial scattering wave function in terms of them. Suppose there is some interatomic distance R_{int} beyond which the channels are essentially uncoupled and V_1 is well described by the van der Waals potential, i.e., the same condition for which Eq. (9) emerged, but still at sufficiently short range such that all channels are locally open. In this intermediate region the radial wave-function matrix can be written in the form

$$F(R) \sim \hat{f}(R) + \hat{g}(R)Y. \quad (29)$$

Here \hat{f} and \hat{g} are diagonal matrices containing the $N = N_o + N_c$ channel reference function and Y is a constant $N \times N$ matrix that plays a similar role to K_{oo} , but in this intermediate region where all channels are locally open. As noted in Sec. III B 2, \hat{f}_i and \hat{g}_i only depend weakly on the collision energy at short range since here $|\bar{E}_i| \ll |V_i^{\text{eff}}(R)|$. Therefore, Y can be considered constant with respect to the collision energy. The energy dependence characteristic of the threshold behavior is instead captured by the QDT parameters, through the transformation (28). As such, once Y is known, computing the physical scattering S matrix at a given energy becomes simply a question of applying the appropriate scattering boundary conditions, as detailed in Ref. [20] and Appendix B 2.

In addition to the open entrance channel $|1, 1\rangle|1, 1\rangle$, the coupled equations (5) include closed channels (four in our case). In the intermediate region, these channels are locally open, so \hat{f} and \hat{g} are defined perfectly well following the prescription in Sec. III B 2. Connecting to the classically forbidden region, where the wave function exponentially decays, introduces a single QDT parameter v_i in each closed channel such that

$$\cos v_i \hat{f}_i - \sin v_i \hat{g}_i \underset{r \rightarrow \infty}{\sim} \frac{e^{-|\bar{k}_i R}}{2\sqrt{|\bar{k}_i|}}, \quad (30)$$

where \hat{f}_i and \hat{g}_i are defined as in Sec. III B 2. This identifies the particular linear combination of \hat{f}_i and \hat{g}_i which is decaying asymptotically.

Given the QDT parameters in each channel, the asymptotic S matrix can be obtained from the Y matrix by applying the appropriate scattering boundary conditions [20]. We start from the Y matrix, which is split into subblocks representing closed and open channels,

$$Y = \begin{bmatrix} Y_{\text{oo}} & Y_{\text{oc}} \\ Y_{\text{co}} & Y_{\text{cc}} \end{bmatrix}. \quad (31)$$

The procedure for eliminating the closed channels to connect Y to long range, where the scattering boundary conditions for the N_o open channels are defined, is described in Appendix B 2. Briefly, this relies on incorporating the effect of the closed channels on the open channels using the reduced Y matrix \bar{Y}_{oo} ,

$$\bar{Y}_{\text{oo}} = Y_{\text{oo}} - Y_{\text{oc}}(\tan \nu + Y_{\text{cc}})^{-1}Y_{\text{co}}, \quad (32)$$

³Formally, $\tan \xi = \frac{\sin(\bar{k}R - \ell\pi/2)\hat{f}(R) - \cos(\bar{k}R - \ell\pi/2)\hat{f}'(R)}{\cos(\bar{k}R - \ell\pi/2)\hat{f}(R) - \sin(\bar{k}R - \ell\pi/2)\hat{f}'(R)} \Big|_{R \rightarrow \infty}$.

where $\tan \nu$ is a diagonal matrix with $\tan \nu_i$ as diagonal elements. Equation (32) therefore folds in the behavior of Feshbach resonances, which arise due to the closed channels and appear as poles when $|\tan \nu + Y_{cc}| \rightarrow 0$. The effective reaction matrix $\bar{\mathbf{R}}$ is given by [see Eq. (B9)]

$$\bar{\mathbf{R}} = \mathbf{C}^{-1}(\bar{\mathbf{Y}}_{oo}^{-1} - \tan \lambda)^{-1} \mathbf{C}^{-1}, \quad (33)$$

where \mathbf{C}^{-1} and $\tan \lambda$ are diagonal matrices containing elements C_i^{-1} and $\tan \lambda_i$. Equation (33) introduces the effects of scattering near threshold, such as a shape resonance. Finally, the \mathbf{S} matrix can be expressed as [see Eq. (B11)]

$$\mathbf{S} = e^{i\xi}(1 + i\bar{\mathbf{R}})(1 - i\bar{\mathbf{R}})^{-1} e^{i\xi}. \quad (34)$$

D. Two-channel model

The general multichannel QDT framework outlined above in Sec. III C can be simplified in the case pertaining to a single open channel, and multiple closed channels over which a single isolated resonance resides. In this case an effective two-channel QDT model captures the essential physics [27,32]. In our model, the open channel o ($i = 1$) is the d -wave entrance channel which contains the shape resonance and the closed channel c ($i = 2$) contains the quasibound state giving rise to the Feshbach resonance. We choose the short-range reference functions such that the \mathbf{Y} matrix is purely off-diagonal

$$\mathbf{Y} = \begin{bmatrix} 0 & y \\ y & 0 \end{bmatrix}, \quad (35)$$

which we are always free to do in the two-channel case [48].

Applying the above MQDT formulas (32) and (33) gives

$$\bar{\mathbf{R}} = \frac{y^2 C^{-2}}{-\tan \nu - y^2 \tan \lambda}, \quad (36)$$

where in our notation we suppress the $i = 1, 2$ indices of the QDT parameters. Writing the \mathbf{S} matrix (in our case just a single complex number) in terms of the scattering phase shift $S = e^{2i\delta_d}$ and using Eq. (34) gives⁴

$$\delta_d = \xi + \arctan \bar{\mathbf{R}}, \quad (37)$$

which yields the scattering phase shift in terms of the QDT parameters

$$\delta_d = \xi + \arctan \left(\frac{y^2 C^{-2}}{-\tan \nu - y^2 \tan \lambda} \right). \quad (38)$$

Using a linear expansion of $\tan \nu$ which goes to zero in the vicinity of a resonance $\tan \nu \approx \frac{\partial \nu}{\partial E} |_{E=E_0} (E - E_0)$ and defining $\frac{1}{2} \bar{\Gamma} = (\frac{\partial \nu}{\partial E} |_{E=E_0})^{-1} y^2$ gives

$$\delta_d = \xi + \arctan \left(\frac{\frac{1}{2} \bar{\Gamma} C^{-2}}{E_0 - E - \frac{1}{2} \bar{\Gamma} \tan \lambda} \right). \quad (39)$$

Comparing the above to Eq. (3), we note that ξ corresponds to our measured background phase shift δ_{bg} .

We now consider the resonance position as a function of the external magnetic field. In the closed channel, the bare bound-state position in energy is $E_0 = \delta\mu(B - B_0)$, where $\delta\mu$

is the difference in magnetic moment between the open and closed channels and B_0 is the field at which the (noninteracting) resonance is at threshold [31]. By defining $\bar{\Gamma}_B = \bar{\Gamma}/\delta\mu$,

$$\delta_d = \delta_{bg} + \arctan \left(\frac{\frac{1}{2} \bar{\Gamma}_B C^{-2}}{B - (B_0 + E/\delta\mu + \frac{1}{2} \bar{\Gamma}_B \tan \lambda)} \right). \quad (40)$$

Within this model, the width and position of the resonance in magnetic field are therefore given by

$$\Gamma_B(E) = C^{-2}(E) \bar{\Gamma}_B, \quad (41)$$

and

$$B_{res}(E) = B_0 + \frac{E}{\delta\mu} + \frac{\bar{\Gamma}_B}{2} \tan \lambda(E), \quad (42)$$

respectively. These formulas elegantly demonstrate the advantage of the MQDT approach. The width of the resonance is factorized into one energy-dependent part associated with the long-range threshold effects, $C^{-2}(E)$, and another energy-independent part $\bar{\Gamma}_B$ associated with the short-range physics. They also demonstrate that threshold effects modify not only the width of a resonance but also its position [25,28,61]. Within Fano's configuration-interaction approach the shift in the resonance position is due to the off-energy shell interactions [62], which have the effect of mixing in the irregular solution to the bare scattering solution in the open channel. Having chosen the reference function f_1 to have a phase that matches the physical background scattering phase shift δ_{bg} in the d -wave channel (i.e., to be the regular solution), the admixture of the irregular solution g is completely captured by $\tan \lambda$ within the QDT formalism, which determines the shift [63].

E. Computations

We now consider the practical computation of the QDT parameters. These can be computed either analytically [22] or numerically [47,64,65]. Here we implement the stable numerical approach developed by Ruzic *et al.* [47]. As discussed by Ruzic *et al.*, reference solutions lose their linear independence when propagating through a centrifugal barrier, so it is optimal to choose reference functions which are purely exponentially growing and decaying in that region. In our case this simply (by construction) corresponds to choosing $\phi_1 = 0$ in Eq. (22), as can be seen in Fig. 5. We then combine this approach with a reference-function rotation to obtain any particular set of reference functions [48,49,66]. This rotation produces QDT parameters corresponding to a different ϕ_1 such that $\xi = \delta_{bg}$ as discussed earlier.

The QDT parameters are computed in the same way as detailed in Ref. [20] and here we just highlight details specific to this work. Numerical propagation of the reference functions was done using Numerov's method [67]. The \hat{f}_1 reference function was propagated out from $R_{min} = 0.1$ to $R_{max} = 25$ using Eq. (21a) as the short-range boundary condition with $\phi_1 = 0$. Matching \hat{f}_1 with f_1 defines ξ_1 via Eq. (17a).³ This also defines the reference function g via Eq. (17b), which serves as a boundary condition to propagate g_1 back to short range. The QDT parameters can be extracted using Eqs. (B2a) and (B2b). These QDT parameters are then rotated [48,49,66]

⁴We note the trigonometric identity $\arctan z = -\frac{i}{2} \ln \left(\frac{1+iz}{1-iz} \right)$.

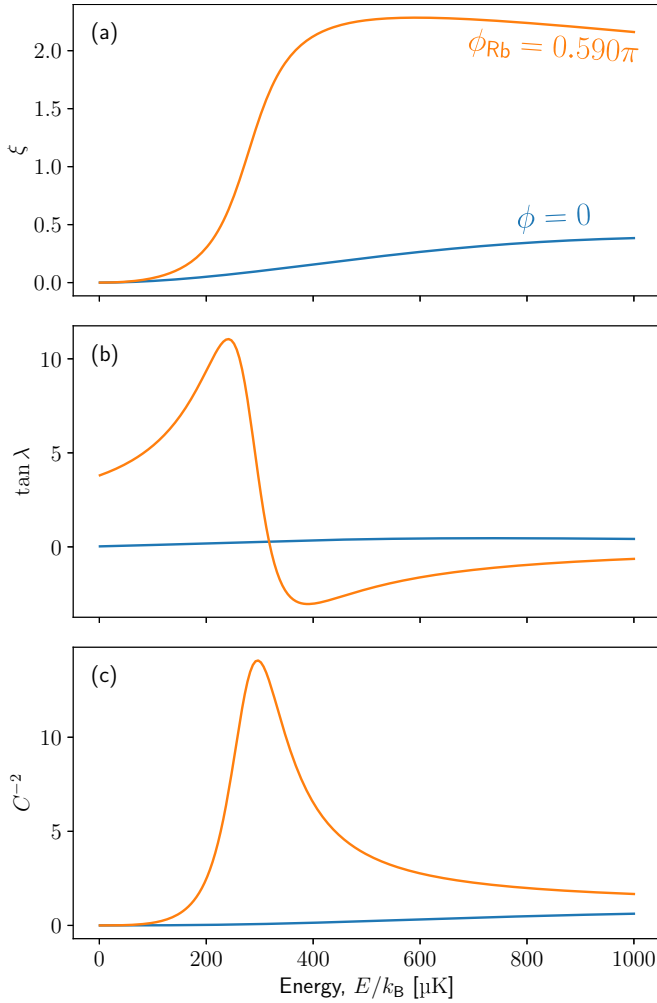


FIG. 6. QDT parameters (a) ξ , (b) $\tan \lambda$, and (c) C^{-2} as a function of energy. The blue lines show numerically calculated parameters using QDT reference functions based on the phase $\phi_1 = 0$ [cf. Eq. (22)]. The orange lines show the QDT parameters transformed to $\phi_1 = 0.590\pi$ using the analytic rotation formulas (B12).

such that $\xi = \delta_{bg}$ following the procedure in Appendix B 3. We note that because ϕ_i is defined at short range (where both the collision energy and the centrifugal term are small compared to the depth of the potential) a single energy independent ϕ_1 will reproduce the energy-dependent δ_{bg} over the entire range of energies we are interested in here.

Figure 6 shows the QDT parameters obtained both as propagated using $\phi_1 = 0$ and following an analytic rotation so that ξ matches the experimentally observed background scattering phase shift. The choice of $\phi_1 = 0$ produces slowly varying QDT parameters, while those rotated to match the physical scattering phase shift show a peak in C^{-2} which directly gives the increased probability of tunneling through the d -wave barrier at the energy of the observed shape resonance.

The QDT parameters are not sensitive to the choice of propagation limits: It is sufficient that at R_{\min} the WKB solution is valid and at R_{\max} the potential has decayed to near zero. The propagation of the reference functions relies only on knowing the reduced mass μ , the van der Waals coefficient C_6 , and the angular momentum ℓ . This means that the QDT

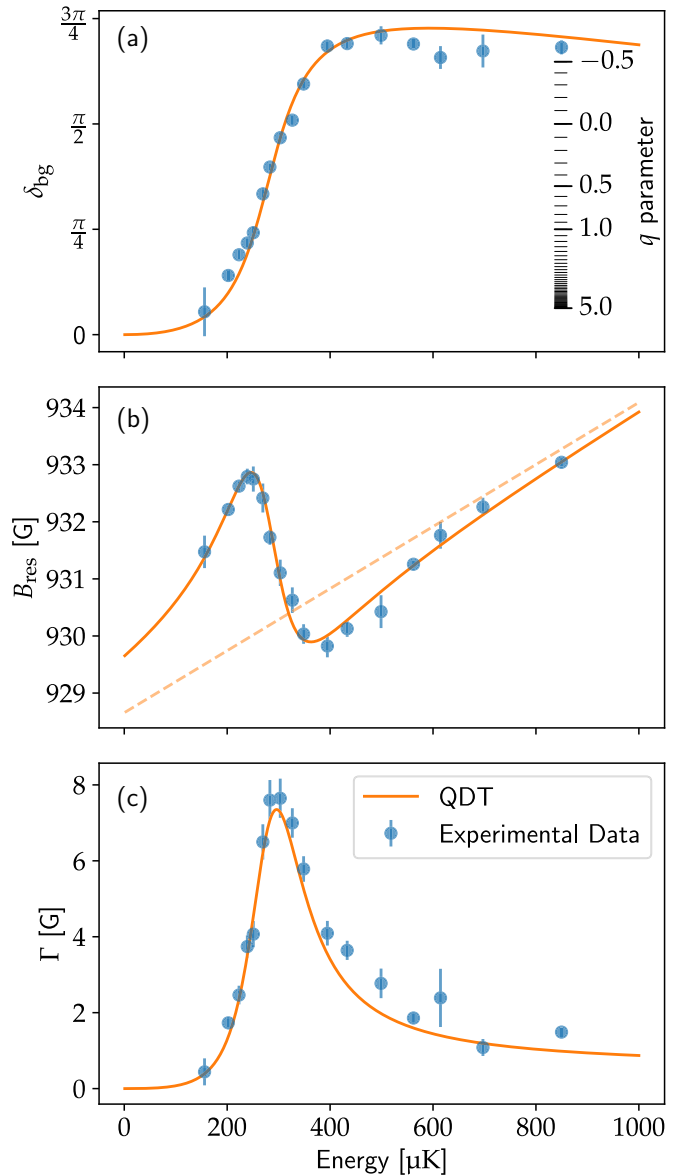


FIG. 7. Properties of the Feshbach resonance as measured at a number of collision energies: (a) the background phase shift and corresponding q parameters, (b) the magnetic field of the resonance, and (c) the width of the resonance. We include predictions from the multichannel quantum defect theory model. The dashed line in (b) indicates the expected position of the Feshbach resonance in the absence of the open-channel effects (shape resonance).

parameters are solely a property of the general long-range potential and account for the threshold effects on the scattering.

IV. RESULTS

For a range of energies, we measure the scattering fraction as a function of magnetic field to obtain scans such as those shown in Fig. 3. From these magnetic field scans we extract the resonance parameters shown in Fig. 7, namely, the background phase δ_{bg} , the resonance position B_{res} , and the resonance width Γ_B , as defined by Eq. (3). These three parameters completely describe the observed resonance

features and their variation captures the interplay between the two resonances.

A. Experimental observations

Figure 7(a) shows the increase of the open-channel d -wave background phase shift across the shape resonance. In particular, we note its transition through the value $\pi/2$ at the location of the shape resonance. During the course of this, the Fano profile undergoes a q reversal which flips the shape of the Fano profiles shown in Fig. 3. The background phase changes by a total value of less than $3\pi/4$ in this system, while an isolated resonance normally accrues a total phase change of π asymptotically, a general feature of resonances in both quantum and classical systems. The discrepancy can be explained by considering that the shape resonance is not a pure isolated Breit-Wigner resonance: Not only are there other resonances in the channel, but in the absence of the shape resonance the background phase shift of the channel would increase [26,28].

Figure 7(b) displays the magnetic field at which the resonance feature is positioned, where we observe a kink in the trajectory, shifting by a substantial fraction of the width of the resonance. Above threshold, a Feshbach resonance usually moves linearly in energy as shown by the dashed line, with the slope given by the difference in magnetic moment between the two channels. The deviation from linear is the manifestation of the interaction between states. Indeed, examples of such behavior were previously found for a Feshbach resonance interacting with an antibound state [43,68] and a p -wave shape resonance [69].

As shown in Fig. 7(c), the Fano profile broadens across the nominal shape resonance energy position by orders of magnitude from the zero-energy width. The Feshbach resonance we inspect is considered narrow [36], and at zero energy the width is limited by the weak s - to d -wave coupling; its observation hence requires a very stable and low noise magnetic field. For experiments conducted above threshold, the Feshbach resonance is, however, readily detected through the shape resonance.

B. QDT analysis

We find the short-range QDT phase $\phi = 0.590\pi$ in the open channel by fitting ξ to the observed background phase in Fig. 7(a). The QDT parameters corresponding to this ϕ are shown in Fig. 6. By fitting Eq. (42) to B_{res} [Fig. 7(b)], we obtain the Feshbach resonance parameters $\bar{\Gamma} = 96 \mu\text{K}$, $\delta\mu = 184 \mu\text{K G}^{-1}$, and $B_0 = 928.7 \text{ G}$.

The width of the resonance predicted by Eq. (41) is shown as an orange line in Fig. 7(c). This is in excellent agreement with the experimental observations and describes the energy dependence of the width entirely through C^{-2} . Since C^{-2} quantifies the tunneling through the centrifugal barrier to short range, we can attribute the broadening of the resonance to the increased amplitude of the wave function at short range due to the shape resonance.

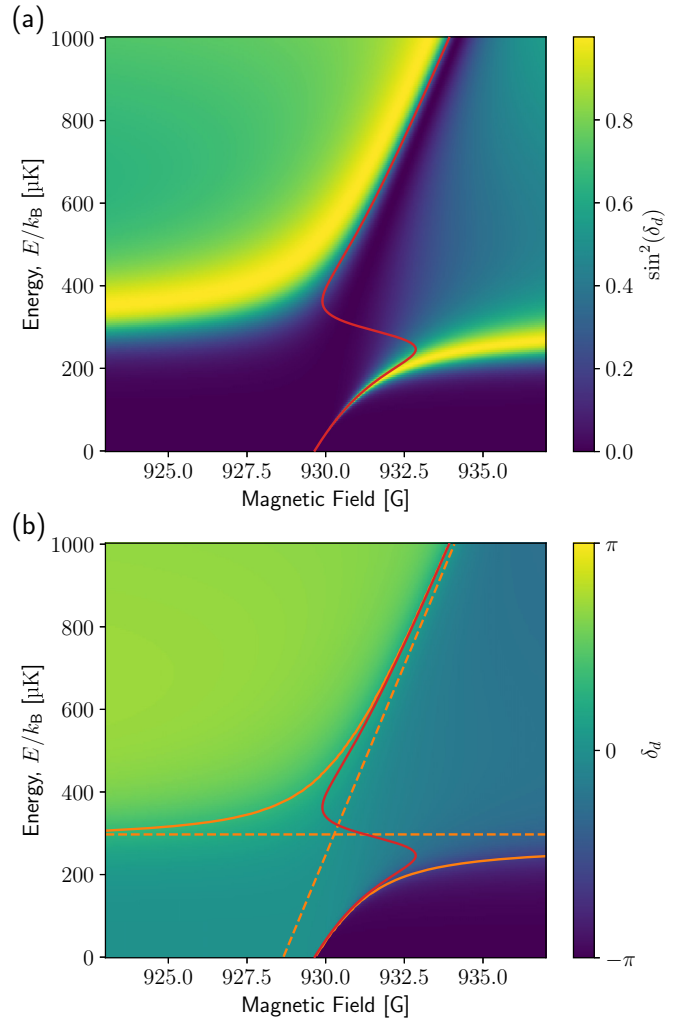


FIG. 8. MQDT calculations in both collision energy and magnetic field: (a) $\sin^2 \delta_d$, which is proportional to the scattering cross section, and (b) the scattering phase shift. In both panels, the position of the Fano resonance in the magnetic field is shown in red, while in (b) the resonance positions in energy are shown as orange solid lines and the noninteracting resonance positions are shown as orange dashed lines.

The shift in B_{res} due to the interaction with the open channel is given by the last term of Eq. (42),

$$\delta B = -\frac{\bar{\Gamma}_B}{2} \tan \lambda(E). \quad (43)$$

The calculated $\tan \lambda$ for this system, shown in Fig. 6(b), explains the nonlinear and nonmonotonic resonance trajectory. We observe that $\tan \lambda$ is nonzero at threshold, so the zero-energy position of the Feshbach resonance is already shifted by $\sim 1 \text{ G}$ due to the coupling to the open channel, that is, due to the presence of the shape resonance. This is particularly apparent in Fig. 7(b), which shows the uncoupled resonance position $B_0 + E/\delta\mu$ as a dashed line.

Figure 8(a) shows the sine squared of the scattering phase shift predicted by the MQDT model, which is proportional to the scattering cross section. The red line shows the predicted position of the Feshbach resonance in the magnetic field [the

orange line in Fig. 7(b)], which can be seen to move between two regions of strong scattering as the energy increases. Resonances are associated with a rapid change in the scattering phase by π . In Fig. 8(b) we present the scattering phase with the positions of the resonances in both the energy and field. We locate resonances in energy by the position at which the change in phase with energy is maximal, i.e.,

$$\left. \frac{\partial^2 \delta}{\partial E^2} \right|_B = 0. \quad (44)$$

These maxima correspond to positions where the phase winds by $\sim \pi$, which is characteristic of a resonance. Similarly, B_{res} corresponds to a winding of π in the field. As is clear from the figure, the positions of the resonances in energy and field do not always line up. In the middle of the kink ($\sim 300 \mu\text{K}$), one encounters a magnetic resonance where there is no resonance in energy. As previously discussed, (energy) resonances arise due to the coupling with a quasibound state near the collision energy. Here, however, one can see that the Fano profile (a dip) arises not from a nearby quasibound state, but from the temporary absence of one. This is discussed in our previous work [35], where we have shown that this occurs as the quasibound states associated with the two resonances undergo an avoided crossing. The lack of correspondence in energy and field positions is also clear from Eqs. (3) and (40): Only B in the denominator changes as a function of magnetic field, giving rise to an isolated Fano profile; in energy, Γ_B , B_{res} , and δ_{bg} all vary rapidly across the shape resonance, leading to a nontrivial winding of the scattering phase. Raoult and Mies [28] state this another way: One cannot always assign a meaningful energy width to a Feshbach resonance due to the energy shift. Here we see the energy shift effectively splits the resonance in two. However, we observe that the Fano profile in the magnetic field is always singular and well defined: The width of the resonance is clear.

V. CONCLUSION

In this work we have studied the nontrivial interplay between a shape resonance and a Feshbach resonance in ultracold atomic ^{87}Rb collisions. By manipulating the collision energy and magnetic field we can tune the shape parameter q of the Fano profile over a range sufficient to observe a full q reversal. In addition to the q reversal we observe strong broadening and an oscillatory kink in the resonance trajectory as the Feshbach resonance moves over the shape resonance.

To explain this behavior, we have presented a multichannel quantum defect theory analysis of the experimental data. The MQDT model is able to accurately capture the essential physics of the interactions over the entire range of energy and magnetic field of interest in terms of just four constants ($\phi = 0.590\pi$, $\bar{\Gamma} = 96 \mu\text{K}$, $\delta\mu = 184 \mu\text{K G}^{-1}$, and $B_0 = 928.7 \text{ G}$) and the three energy-dependent QDT parameters (C^{-2} , $\tan \lambda$, and ξ), which are simply properties of the long-range van der Waals potential.

We observed an excellent match between experiment and theoretical predictions, and the MQDT framework demonstrated that the observed resonance behavior is primarily due to the open channel, related to the short-range enhancement (determined by C^{-2}) and long-range phase rotation

(determined by $\tan \lambda$) of the scattering wave function. In addition to providing additional insight, MQDT also proves a vastly simpler tool than complete coupled-channel calculations, which require a complex multichannel potential.

Our experimental scheme using an optical collider implements a Feshbach resonance “microscope” which magnifies a narrow zero-energy feature through a shape resonance. Threshold behavior dictates that an isolated Feshbach resonance will generally broaden as its position is tuned towards higher energies with a magnetic field [70]. The shape resonance expedites this broadening while maximizing the number of scattered particles and the signal-to-noise ratio for the measurement. While for our particular realization the Feshbach resonance in question can be observed close to threshold, in the future the approach may be used to verify predicted ultranarrow Feshbach resonances that evade experimental observation in conventional loss spectroscopy.

ACKNOWLEDGMENTS

This work was supported by the Marsden Fund of New Zealand (Contract No. UOO1923). J.F.E.C. acknowledges a Dodd-Walls Fellowship and M.C. a University of Otago Postgraduate Publishing Bursary (Doctoral).

APPENDIX A: LOSS SPECTROSCOPY

We measure the (near) zero-energy position of the Feshbach resonance by observing the effect of a magnetic field on a stationary atomic cloud. At the Feshbach resonance, the scattering length between the ^{87}Rb atoms diverges, resulting in an increased three-body loss rate.

The procedure for performing loss spectroscopy measurement is initially identical to that laid out in Sec. II, up to the point where we would split and collide the clouds of atoms. Instead, a single cloud which has been further evaporatively cooled below 400 nK is held in a stationary optical dipole trap and exposed to a magnetic field for 200 ms. An absorption image of the single cloud is then used to estimate the number of atoms remaining in the trap. In such an experiment, the profile of the atom loss can often be well approximated by

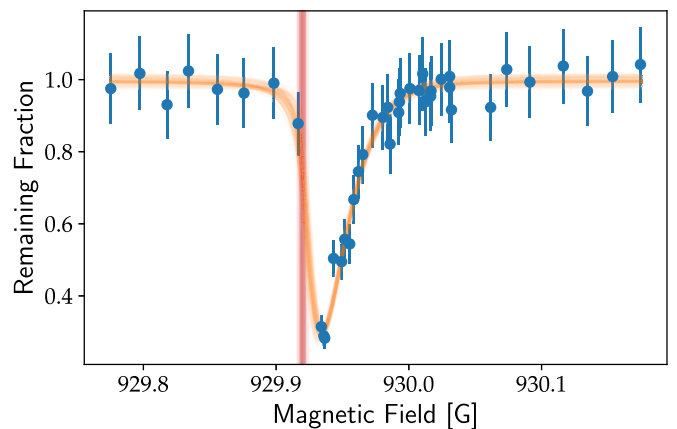


FIG. 9. Representative measurement of the atom loss fitted by the described model. The extracted resonance position is shown in red.

a Gaussian line shape [36], especially when the width of the Feshbach resonance is greater than the range of collision energies present in a thermal cloud. In our data, we observe an asymmetry that is distinctly non-Gaussian (shown in Fig. 9), requiring us to take into account the thermal distribution of the finite-temperature cloud; the Maxwell-Boltzmann distribution is skewed towards high energies with negative energies forbidden and the same skew is imposed upon the shape of the atom loss in the magnetic field as the resonance tunes above threshold. Explicitly, we model the coupling rate to the Feshbach state as a Breit-Wigner profile in energy,

$$R(E, B) \propto \frac{\gamma}{\gamma^2 + [E - \epsilon(B)]^2}, \quad (\text{A1})$$

for atoms at a given energy E , when the Feshbach resonance is at energy $\epsilon(B) = \delta\mu(B - B_0)$. The distribution of kinetic energies (which are strictly positive) are taken to be Maxwellian at a temperature T :

$$P(T, E) = kT e^{-E/kT}. \quad (\text{A2})$$

The three-body loss rate K_3 is then proportional to the integral of these over energy,

$$K_3(B) \propto \int_0^\infty R(E, B) P(T, E) dE. \quad (\text{A3})$$

If we assume that the loss process does not produce evaporative heating or cooling and that the loss rate from other processes is negligible, then the loss can be modeled by

$$\dot{N}(B) = -K_3(B)N^2, \quad (\text{A4})$$

where N is the number of atoms remaining. Here we are describing the three-body loss process as second order in atom number (akin to a two-body loss process) to encapsulate the inverse density and hence N^{-1} atom number dependence of K_3 [71]. A fit of this model to experimental data is shown in Fig. 9, and a number of such measurements give us an estimate of the zero-energy Feshbach resonance position $B_0 = 929.918(6)$ G.

APPENDIX B: QDT SUPPLEMENTARY

1. Calculating QDT parameters

Abel's identity implies that the Wronskian W of any pair of solutions to Eq. (10) is a constant independent of R . By considering Wronskians of appropriate combinations of the QDT reference functions $\{f_i, g_i, \hat{f}_i, \hat{g}_i\}$, expressions for the QDT parameters can be obtained [20,47]. For example, from Eq. (28) and $W(\hat{g}_i, \hat{f}_i) = 1$ and $W(\hat{g}_i, \hat{g}_i) = 0$,

$$W(\hat{g}_i, f_i) = C_i^{-1}, \quad (\text{B1a})$$

$$W(\hat{g}_i, g_i) = C_i \tan \lambda_i, \quad (\text{B1b})$$

and evaluations around $R \simeq R_m$ and in the limit $R \rightarrow \infty$ give

$$C_i^{-2} = [W(\hat{g}_i, f_i)]^2 = \begin{cases} \bar{k}_i(R) f_i^2(R) + f_i^2(R) / \bar{k}_i(R) & \text{for } R \simeq R_m \\ [\bar{k}_i \hat{f}_i^2(R) + \hat{f}_i^2(R) / \bar{k}_i]^{-1} & \text{for } R \rightarrow \infty, \end{cases} \quad (\text{B2a})$$

$$\tan \lambda_i = C_i^{-1} W(\hat{g}_i, g_i) = \begin{cases} \bar{k}_i(R) f_i(R) g_i(R) + f_i'(R) g_i'(R) / \bar{k}_i(R) & \text{for } R \simeq R_m \\ -C_i^{-2} [\bar{k}_i \hat{f}_i(R) \hat{g}_i(R) + \hat{f}_i'(R) \hat{g}_i'(R) / \bar{k}_i] & \text{for } R \rightarrow \infty. \end{cases} \quad (\text{B2b})$$

2. Open-channel elimination in MQDT and expression of the S matrix

In this section we relate the constant $N \times N$, Y matrix introduced in Eq. (29) to the $N_o \times N_o$, S matrix [20,72].

As discussed in Sec. III C, a solution matrix to the coupled-channel problem over some (intermediate) short range can be expressed through the QDT reference functions \hat{f}_i and \hat{g}_i as

$$F = \hat{f} + \hat{g}Y, \quad (\text{B3})$$

where Y is a constant matrix. This is possible because at this intermediate range (cf. Sec. III C), where the boundary conditions define the $N \times N$ diagonal matrices \hat{f} and \hat{g} , all N channels are locally open, even the N_c channels that are asymptotically closed.

To obtain the N_o physically meaningful solutions, the closed channels need to be eliminated from Eq. (B3). This elimination can be done by considering a transformation T that builds a reduced $N \times N_o$ solution matrix \bar{F} out of F , where each of the N_o columns of \bar{F} is a linear combination of the N columns of F ,

$$\begin{aligned} \begin{bmatrix} \bar{F}_{oo} \\ \bar{F}_{co} \end{bmatrix} &= \begin{bmatrix} \hat{f}_{oo} & 0 \\ 0 & \hat{f}_{cc} \end{bmatrix} + \begin{bmatrix} \hat{g}_{oo} & 0 \\ 0 & \hat{g}_{cc} \end{bmatrix} \begin{bmatrix} Y_{oo} & Y_{oc} \\ Y_{co} & Y_{cc} \end{bmatrix} \begin{bmatrix} T_{oo} \\ T_{co} \end{bmatrix} \\ &= \begin{bmatrix} \hat{f}_{oo} T_{oo} + \hat{g}_{oo} (Y_{oo} T_{oo} + Y_{oc} T_{co}) \\ \hat{f}_{cc} T_{co} + \hat{g}_{cc} (Y_{co} T_{oo} + Y_{cc} T_{co}) \end{bmatrix} \\ &= \begin{bmatrix} \hat{f}_{oo} + \hat{g}_{oo} \bar{Y}_{oo} \\ -(\hat{f}_{cc} - \tan \nu_{cc} \hat{g}_{cc}) (\tan \nu_{cc} + Y_{cc})^{-1} Y_{co} \end{bmatrix}, \end{aligned} \quad (\text{B4})$$

$\underset{\sim}{\underset{R \rightarrow \infty}{0}}$, cf. Eq. (30)

where in order to obtain the last step the blocks of \mathbf{T} are chosen as $\mathbf{T}_{oo} = 1$ and $\mathbf{T}_{co} = -(\tan \nu_{cc} + \mathbf{Y}_{cc})^{-1} \mathbf{Y}_{co}$ and we introduced the reduced \mathbf{Y} matrix $\bar{\mathbf{Y}}_{oo} = \mathbf{Y}_{oo} \mathbf{T}_{oo} + \mathbf{Y}_{oc} \mathbf{T}_{co}$, which can be cast as Eq. (32). The blocks of the resulting reduced solution matrix fulfill

$$\bar{\mathbf{F}}_{oo} = \hat{\mathbf{f}}_{oo} + \hat{\mathbf{g}}_{oo} \bar{\mathbf{Y}}_{oo}, \quad (\text{B5a})$$

$$\bar{\mathbf{F}}_{co} \underset{R \rightarrow \infty}{\sim} 0 \quad (\text{B5b})$$

and the closed channels have been eliminated. Equation (B5a) expresses the open-open block of the reduced solution matrix $\bar{\mathbf{F}}_{oo}$ in terms of the short-range reference functions $\hat{\mathbf{f}}_i$ and $\hat{\mathbf{g}}_i$. However, to make the connection to the physical \mathbf{S} matrix we want a solution of the form

$$\mathbf{F}_{oo} \sim \mathbf{f} + \mathbf{g} \bar{\mathbf{R}}, \quad (\text{B6})$$

based on the energy-normalized asymptotic reference functions f_i and g_i . Here $\bar{\mathbf{R}}$ constitutes an effective reaction matrix with the “true” reaction matrix (often called K or R in the literature) being defined by a form identical to Eq. (B6), but with the QDT reference solutions f_i and g_i replaced with the appropriate spherical Bessel function solutions [cf. Eq. (6)].

The relations between the short- and long-range reference functions are [Eq. (28)]

$$\hat{\mathbf{f}}_{oo} = \mathbf{C} \mathbf{f}_{oo}, \quad (\text{B7a})$$

$$\hat{\mathbf{g}}_{oo} = \mathbf{C}^{-1} \mathbf{g}_{oo} - \tan \lambda \mathbf{C} \mathbf{f}_{oo}, \quad (\text{B7b})$$

and inserting Eqs. (B7) into Eq. (B5a) gives

$$\bar{\mathbf{F}}_{oo} = \mathbf{C} \mathbf{f}_{oo} + (\mathbf{C}^{-1} \mathbf{g}_{oo} - \tan \lambda \mathbf{C} \mathbf{f}_{oo}) \bar{\mathbf{Y}}_{oo} = \mathbf{f}_{oo} \mathbf{C} (1 - \tan \lambda \bar{\mathbf{Y}}_{oo}) + \mathbf{g}_{oo} \mathbf{C}^{-1} \bar{\mathbf{Y}}_{oo}. \quad (\text{B8})$$

Multiplying from the right by $\mathbf{C} (1 - \tan \lambda \bar{\mathbf{Y}}_{oo})^{-1}$, a transformed solution matrix of the desired form (B6) is obtained:

$$\bar{\mathbf{F}}_{oo} = \mathbf{f}_{oo} + \mathbf{g}_{oo} \underbrace{\mathbf{C}^{-1} (\bar{\mathbf{Y}}_{oo}^{-1} - \tan \lambda)^{-1} \mathbf{C}^{-1}}_{\bar{\mathbf{R}}}. \quad (\text{B9})$$

Using the asymptotic properties of f_i and g_i [cf. Eqs. (17)], this solution can be expanded as

$$\bar{\mathbf{F}}_{oo} \underset{R \rightarrow \infty}{\sim} \frac{e^{i(kR - \ell\pi/2 + \xi)} - e^{-i(kR - \ell\pi/2 + \xi)}}{2i} + \frac{e^{i(kR - \ell\pi/2 + \xi)} + e^{-i(kR - \ell\pi/2 + \xi)}}{2} \bar{\mathbf{R}} \sim e^{-i(kR - \ell\pi/2)} e^{-i\xi} (1 - i\bar{\mathbf{R}}) + e^{i(kR - \ell\pi/2)} e^{i\xi} (1 + i\bar{\mathbf{R}}), \quad (\text{B10})$$

and by multiplying from the right by $(1 - i\bar{\mathbf{R}})^{-1} e^{i\xi}$, a solution form with incoming and outgoing spherical wave components is obtained:

$$\bar{\mathbf{F}}_{oo} \underset{R \rightarrow \infty}{\sim} \underbrace{e^{-i(kR - \ell\pi/2)}}_{\text{incoming}} + \underbrace{e^{i(kR - \ell\pi/2)}}_{\text{outgoing}} \overbrace{e^{i\xi} (1 + i\bar{\mathbf{R}}) (1 - i\bar{\mathbf{R}})^{-1} e^{i\xi}}^{\mathbf{S}}. \quad (\text{B11})$$

In particular, it provides us with the desired expression of \mathbf{S} , Eq. (34).

3. Rotation of QDT parameters

Once the QDT parameters have been calculated for $\phi = 0$, it is straightforward to analytically obtain them for any particular choice of ϕ by using the transformations [66]

$$\bar{\xi} = \arctan \left[\frac{C^2 \sin \xi (\cos \phi + \tan \lambda \sin \phi) - \cos \xi \sin \phi}{C^2 \cos \xi (\cos \phi + \tan \lambda \sin \phi) + \sin \xi \sin \phi} \right], \quad (\text{B12a})$$

$$\tan \bar{\lambda} = - \frac{2C^4 \tan \lambda \cos 2\phi + [1 + C^4 (\tan^2 \lambda - 1)] \sin 2\phi}{2C^4 \cos^2 \phi + 2 \sin \phi [\sin \phi + C^4 \tan \lambda (2 \cos \phi + \tan \lambda \sin \phi)]}, \quad (\text{B12b})$$

$$\bar{C} = \left[\frac{\sin \xi \sin \phi}{C} + C \cos \xi (\cos \phi + \tan \lambda \sin \phi) \right] \sqrt{1 + \frac{[\cos \xi \sin \phi - C^2 \sin \xi (\cos \phi + \tan \lambda \sin \phi)]^2}{[\sin \xi \sin \phi + C^2 \cos \xi (\cos \phi + \tan \lambda \sin \phi)]^2}}, \quad (\text{B12c})$$

$$\bar{\nu} = \nu - \phi. \quad (\text{B12d})$$

- [1] E. A. Donley, N. R. Claussen, S. L. Cornish, J. L. Roberts, E. A. Cornell, and C. E. Wieman, Dynamics of collapsing and exploding Bose–Einstein condensates, *Nature (London)* **412**, 295 (2001).
- [2] C. A. Regal, M. Greiner, and D. S. Jin, Observation of Resonance Condensation of Fermionic Atom Pairs, *Phys. Rev. Lett.* **92**, 040403 (2004).
- [3] M. W. Zwierlein, C. A. Stan, C. H. Schunck, S. M. F. Raupach, A. J. Kerman, and W. Ketterle, Condensation of Pairs of Fermionic Atoms near a Feshbach Resonance, *Phys. Rev. Lett.* **92**, 120403 (2004).
- [4] C. R. Cabrera, L. Tanzi, J. Sanz, B. Naylor, P. Thomas, P. Cheiney, and L. Tarruell, Quantum liquid droplets in a mixture of Bose–Einstein condensates, *Science* **359**, 301 (2018).
- [5] K.-K. Ni, S. Ospelkaus, M. H. G. de Miranda, A. Pe’er, B. Neyenhuis, J. J. Zirbel, S. Kotochigova, P. S. Julienne, D. S. Jin, and J. Ye, A high phase-space-density gas of polar molecules, *Science* **322**, 231 (2008).
- [6] J. G. Danzl, E. Haller, M. Gustavsson, M. J. Mark, R. Hart, N. Bouloufa, O. Dulieu, H. Ritsch, and H.-C. Nägerl, Quantum gas of deeply bound ground state molecules, *Science* **321**, 1062 (2008).
- [7] P. D. Gregory, J. A. Blackmore, S. L. Bromley, and S. L. Cornish, Loss of Ultracold $^{87}\text{Rb}^{133}\text{Cs}$ Molecules Via Optical Excitation of Long-Lived Two-Body Collision Complexes, *Phys. Rev. Lett.* **124**, 163402 (2020).
- [8] R. Bause, A. Schindewolf, R. Tao, M. Duda, X.-Y. Chen, G. Quéméner, T. Karman, A. Christianen, I. Bloch, and X.-Y. Luo, Collisions of ultracold molecules in bright and dark optical dipole traps, *Phys. Rev. Research* **3**, 033013 (2021).
- [9] P. Gersema, K. K. Voges, M. Meyer zum Alten Borgloh, L. Koch, T. Hartmann, A. Zenesini, S. Ospelkaus, J. Lin, J. He, and D. Wang, Probing Photoinduced Two-Body Loss of Ultracold Nonreactive Bosonic $^{23}\text{Na}^{87}\text{Rb}$ and $^{23}\text{Na}^{39}\text{K}$ Molecules, *Phys. Rev. Lett.* **127**, 163401 (2021).
- [10] M. Mayle, G. Quéméner, B. P. Ruzic, and J. L. Bohn, Scattering of ultracold molecules in the highly resonant regime, *Phys. Rev. A* **87**, 012709 (2013).
- [11] J. F. E. Croft, J. L. Bohn, and G. Quéméner, Unified model of ultracold molecular collisions, *Phys. Rev. A* **102**, 033306 (2020).
- [12] J. F. E. Croft, J. L. Bohn, and G. Quéméner, Anomalous lifetimes of ultracold complexes decaying into a single channel: What’s taking so long in there? [arXiv:2111.09956](https://arxiv.org/abs/2111.09956).
- [13] A. Christianen, G. C. Groenenboom, and T. Karman, Lossy quantum defect theory of ultracold molecular collisions, *Phys. Rev. A* **104**, 043327 (2021).
- [14] A. Frisch, M. Mark, K. Aikawa, F. Ferlaino, J. L. Bohn, C. Makrides, A. Petrov, and S. Kotochigova, Quantum chaos in ultracold collisions of gas-phase erbium atoms, *Nature (London)* **507**, 475 (2014).
- [15] G. Durastante, C. Politi, M. Sohmen, P. Ilzhöfer, M. J. Mark, M. A. Norcia, and F. Ferlaino, Feshbach resonances in an erbium-dysprosium dipolar mixture, *Phys. Rev. A* **102**, 033330 (2020).
- [16] M. J. Seaton, Quantum defect theory I. General formulation, *Proc. Phys. Soc.* **88**, 801 (1966).
- [17] C. Greene, U. Fano, and G. Strinati, General form of the quantum-defect theory, *Phys. Rev. A* **19**, 1485 (1979).
- [18] F. Mies, A scattering theory of diatomic molecules, *Mol. Phys.* **41**, 953 (1980).
- [19] C. H. Greene, A. R. P. Rau, and U. Fano, General form of the quantum-defect theory. II, *Phys. Rev. A* **26**, 2441 (1982).
- [20] F. H. Mies, A multichannel quantum defect analysis of diatomic predissociation and inelastic atomic scattering, *J. Chem. Phys.* **80**, 2514 (1984).
- [21] B. Gao, Quantum-defect theory of atomic collisions and molecular vibration spectra, *Phys. Rev. A* **58**, 4222 (1998).
- [22] B. Gao, Solutions of the Schrödinger equation for an attractive $1/r^6$ potential, *Phys. Rev. A* **58**, 1728 (1998).
- [23] B. Gao, Theory of slow-atom collisions, *Phys. Rev. A* **54**, 2022 (1996).
- [24] J. P. Burke, C. H. Greene, and J. L. Bohn, Multichannel Cold Collisions: Simple Dependences on Energy and Magnetic Field, *Phys. Rev. Lett.* **81**, 3355 (1998).
- [25] F. H. Mies and M. Raoult, Analysis of threshold effects in ultracold atomic collisions, *Phys. Rev. A* **62**, 012708 (2000).
- [26] H. R. Sadeghpour, J. L. Bohn, M. J. Cavagnero, B. D. Esry, I. I. Fabrikant, J. H. Macek, and A. R. P. Rau, Collisions near threshold in atomic and molecular physics, *J. Phys. B* **33**, R93 (2000).
- [27] F. H. Mies, E. Tiesinga, and P. S. Julienne, Manipulation of Feshbach resonances in ultracold atomic collisions using time-dependent magnetic fields, *Phys. Rev. A* **61**, 022721 (2000).
- [28] M. Raoult and F. H. Mies, Feshbach resonance in atomic binary collisions in the Wigner threshold law regime, *Phys. Rev. A* **70**, 012710 (2004).
- [29] P. S. Julienne and B. Gao, in *Proceedings of the XXth International Conference on Atomic Physics, Innsbruck, 2006*, edited by C. Roos, H. Häffner, and R. Blatt, AIP Conf. Proc. No. 869 (AIP, Melville, 2006), p. 261.
- [30] P. S. Julienne, Ultracold molecules from ultracold atoms: A case study with the KRb molecule, *Faraday Discuss.* **142**, 361 (2009).
- [31] C. Chin, R. Grimm, P. Julienne, and E. Tiesinga, Feshbach resonances in ultracold gases, *Rev. Mod. Phys.* **82**, 1225 (2010).
- [32] K. Jachymski and P. S. Julienne, Analytical model of overlapping Feshbach resonances, *Phys. Rev. A* **88**, 052701 (2013).
- [33] Y. Cui, C. Shen, M. Deng, S. Dong, C. Chen, R. Lü, B. Gao, M. K. Tey, and L. You, Observation of Broad d -Wave Feshbach Resonances with a Triplet Structure, *Phys. Rev. Lett.* **119**, 203402 (2017).
- [34] X.-C. Yao, R. Qi, X.-P. Liu, X.-Q. Wang, Y.-X. Wang, Y.-P. Wu, H.-Z. Chen, P. Zhang, H. Zhai, Y.-A. Chen, and J.-W. Pan, Degenerate Bose gases near a d -wave shape resonance, *Nat. Phys.* **15**, 570 (2019).
- [35] M. Chilcott, R. Thomas, and N. Kjørsgaard, Experimental observation of the avoided crossing of two S -matrix resonance poles in an ultracold atom collider, *Phys. Rev. Research* **3**, 033209 (2021).
- [36] A. Marte, T. Volz, J. Schuster, S. Dürr, G. Rempe, E. G. M. van Kempen, and B. J. Verhaar, Feshbach Resonances in Rubidium 87: Precision Measurement and Analysis, *Phys. Rev. Lett.* **89**, 283202 (2002).
- [37] N. R. Thomas, N. Kjørsgaard, P. S. Julienne, and A. C. Wilson, Imaging of s and d Partial-Wave Interference in Quantum Scattering of Identical Bosonic Atoms, *Phys. Rev. Lett.* **93**, 173201 (2004).

- [38] C. Buggle, J. Léonard, W. von Klitzing, and J. T. M. Walraven, Interferometric Determination of the s and d -Wave Scattering Amplitudes in ^{87}Rb , *Phys. Rev. Lett.* **93**, 173202 (2004).
- [39] M. Eisele, In situ beobachtung von Feshbach-resonanzen mittels photoassoziativer ionisation, Ph.D. thesis, Universität Tübingen, 2021.
- [40] C. S. Chisholm, R. Thomas, A. B. Deb, and N. Kjærgaard, A three-dimensional steerable optical tweezer system for ultracold atoms, *Rev. Sci. Instrum.* **89**, 103105 (2018).
- [41] R. Thomas and N. Kjærgaard, A digital feedback controller for stabilizing large electric currents to the ppm level for Feshbach resonance studies, *Rev. Sci. Instrum.* **91**, 034705 (2020).
- [42] N. Kjærgaard, A. S. Mellish, and A. C. Wilson, Differential scattering measurements from a collider for ultracold atoms, *New J. Phys.* **6**, 146 (2004).
- [43] R. Thomas, M. Chilcott, E. Tiesinga, A. B. Deb, and N. Kjærgaard, Observation of bound state self-interaction in a nano-eV atom collider, *Nat. Commun.* **9**, 4895 (2018).
- [44] A. E. Miroshnichenko, S. Flach, and Y. S. Kivshar, Fano resonances in nanoscale structures, *Rev. Mod. Phys.* **82**, 2257 (2010).
- [45] U. Fano and A. R. P. Rau, *Atomic Collisions and Spectra* (Academic, London, 1986).
- [46] A. R. P. Rau, Perspectives on the Fano resonance formula, *Phys. Scr.* **69**, C10 (2004).
- [47] B. P. Ruzic, C. H. Greene, and J. L. Bohn, Quantum defect theory for high-partial-wave cold collisions, *Phys. Rev. A* **87**, 032706 (2013).
- [48] A. Giusti-Suzor and U. Fano, Alternative parameters of channel interactions. I. Symmetry analysis of the two-channel coupling, *J. Phys. B* **17**, 215 (1984).
- [49] R. Osséni, O. Dulieu, and M. Raoult, Optimization of generalized multichannel quantum defect reference functions for Feshbach resonance characterization, *J. Phys. B* **42**, 185202 (2009).
- [50] A. Pashov, O. Docenko, M. Tamanis, R. Ferber, H. Knöckel, and E. Tiemann, Coupling of the $X^1\sigma^+$ and $a^3\sigma^+$ states of KRb, *Phys. Rev. A* **76**, 022511 (2007).
- [51] F. H. Mies and P. S. Julienne, A multichannel quantum defect analysis of two-state couplings in diatomic molecules, *J. Chem. Phys.* **80**, 2526 (1984).
- [52] D. E. Manolopoulos, An improved log derivative method for inelastic scattering, *J. Chem. Phys.* **85**, 6425 (1986).
- [53] A. E. Thornley and J. M. Hutson, Bound-state wave functions from coupled channel calculations using log-derivative propagators: Application to spectroscopic intensities in Ar–HF, *J. Chem. Phys.* **101**, 5578 (1994).
- [54] E. Tiesinga, C. J. Williams, P. S. Julienne, K. M. Jones, P. D. Lett, and W. D. Phillips, A spectroscopic determination of scattering lengths for sodium atom collisions, *J. Res. Natl. Inst. Stand. Technol.* **101**, 505 (1996).
- [55] J. M. Hutson, in *Cold Molecules: Theory, Experiment, Applications*, edited by R. Krems, B. Friedrich, and W. C. Stwalley (CRC, Boca Raton, 2009), Chap. 1.
- [56] P. G. Burke, *R-Matrix Theory of Atomic Collisions* (Springer, Berlin, 2013).
- [57] H. Friedrich, *Scattering Theory*, 2nd ed. (Springer, Berlin, 2015).
- [58] H. T. C. Stoof, J. M. V. A. Koelman, and B. J. Verhaar, Spin-exchange and dipole relaxation rates in atomic hydrogen: Rigorous and simplified calculations, *Phys. Rev. B* **38**, 4688 (1988).
- [59] A. Derevianko, J. F. Babb, and A. Dalgarno, High-precision calculations of van der Waals coefficients for heteronuclear alkali-metal dimers, *Phys. Rev. A* **63**, 052704 (2001).
- [60] M. Abramowitz and I. A. Stegun, *Handbook of Mathematical Functions* (Dover, New York, 1970).
- [61] P. Naidon and L. Pricoupenko, Width and shift of Fano-Feshbach resonances for van der Waals interactions, *Phys. Rev. A* **100**, 042710 (2019).
- [62] U. Fano, Effects of configuration interaction on intensities and phase shifts, *Phys. Rev.* **124**, 1866 (1961).
- [63] U. Fano, Connection between configuration-mixing and quantum-defect treatments, *Phys. Rev. A* **17**, 93 (1978), qdt.
- [64] B. Yoo and C. H. Greene, Implementation of the quantum-defect theory for arbitrary long-range potentials, *Phys. Rev. A* **34**, 1635 (1986).
- [65] J. F. E. Croft, A. O. G. Wallis, J. M. Hutson, and P. S. Julienne, Multichannel quantum defect theory for cold molecular collisions, *Phys. Rev. A* **84**, 042703 (2011).
- [66] J. F. E. Croft, J. M. Hutson, and P. S. Julienne, Optimized multichannel quantum defect theory for cold molecular collisions, *Phys. Rev. A* **86**, 022711 (2012).
- [67] B. V. Noumerov, A method of extrapolation of perturbations, *Mon. Not. R. Astron. Soc.* **84**, 592 (1924).
- [68] B. Marcelis, E. G. M. van Kempen, B. J. Verhaar, and S. J. J. M. F. Kokkelmans, Feshbach resonances with large background scattering length: Interplay with open-channel resonances, *Phys. Rev. A* **70**, 012701 (2004).
- [69] D. J. M. Ahmed-Braun, K. G. Jackson, S. Smale, C. J. Dale, B. A. Olsen, S. J. J. M. F. Kokkelmans, P. S. Julienne, and J. H. Thywissen, Probing open- and closed-channel p -wave resonances, *Phys. Rev. Research* **3**, 033269 (2021).
- [70] M. S. J. Horvath, R. Thomas, E. Tiesinga, A. B. Deb, and N. Kjærgaard, Above-threshold scattering about a Feshbach resonance for ultracold atoms in an optical collider, *Nat. Commun.* **8**, 452 (2017).
- [71] Q. Beaufils, A. Crubellier, T. Zanon, B. Laburthe-Tolra, E. Maréchal, L. Vernac, and O. Gorceix, Feshbach resonance in d -wave collisions, *Phys. Rev. A* **79**, 032706 (2009).
- [72] B. P. Ruzic, Exploring exotic atomic and molecular collisions at ultracold temperatures, Ph.D. thesis, University of Colorado at Boulder, 2015.